CHEMISTRY OF MATERIALS

pubs.acs.org/cm

Article

Second-Harmonic Generation Response in Nitridophosphates MP_2N_4 (M = Ge, Sn, Pb) and the Role of Stereochemically Active Lone Pairs

Xiyue Cheng,* Victor Trinquet, Bohan Ding, Gian-Marco Rignanese, Xavier Gonze, and Shuiquan Deng*

Cite This: *Chem. Mater.* 2025, 37, 3709−3719

Read Online

ACCESS | Metrics & More | Article Recommendations | Supporting Information

ABSTRACT: The recent synthesis of two noncentrosymmetric (NCS) nitridophosphates, GeP_2N_4 and $Sn_6[P_{12}N_{24}]$, featuring stereochemically active lone pairs (SCALPs), provides an opportunity to explore their role in nonlinear optical (NLO) properties and assess the potential of nitridophosphates for NLO applications. Through high-throughput screening of all nitridophosphate compounds in the Materials Project database and Inorganic Crystal Structure Database, we identify 23 NCS nitridophosphates with nonzero second-harmonic generation (SHG) responses. In comparison, MP_2N_4 (M = Ge, Sn, Pb) family, in both $Pna2_1$ and $R3m$ structures, emerges as the only nitridophosphates that combines significant SHG response and sizable birefringence within a band gap range suitable for infrared NLO applications. First-principles calculations reveal that $Pna2_1$ phases of MP_2N_4 generally exhibit larger SHG responses than the $R3m$ ones and substituting Ge^{2+} with more polarizable Sn^{2+} or Pb^{2+} enhances the SHG response to 4.1 and 7.2 pm/V (∼12 and 22 × KDP), respectively. Our atom response theory analysis indicates that the SHG response is predominantly driven by nonbonding N 2p states, while SCALPs provide a positive but secondary contribution, as the SHG magnitude inversely correlates with SCALP strength. Additionally, we reveal that $NaPN_2$ and HPN_2 exhibit impressive SHG response (∼10 × KDP) combined with remarkable band gaps exceeding 6.2 eV, making them promising candidates for ultraviolet (UV) or visible NLO applications. This study sheds light on the mechanisms driving the NLO behavior in MP_2N_4 and highlights nitridophosphates as a promising platform for developing advanced NLO materials.

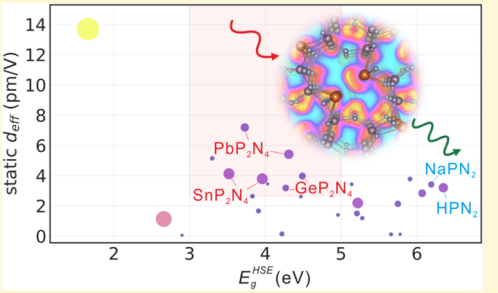

1. INTRODUCTION

Second-harmonic generation (SHG) arising in second-order nonlinear optical (NLO) crystal materials enables the effective doubling of laser frequency, facilitating wavelength conversion and phase modulation.[1,2] These materials serve as essential components in all-solid-state lasers, playing a fundamental and critical role in various applications, including laser manufacturing, laser communications and medical technologies.[3−11] Despite extensive research efforts over the past several decades aimed at discovering high-performance NLO materials across a diverse category of compounds—such as borates, chalcogenides, iodates, halides, and hybrid materials—only a limited number of candidates fulfill the criteria for practical applications. Notable examples include β-BBO (β-BaB_2O_4),[12] LBO (LiB_3O_5)[13] as ultraviolet (UV) to deep UV NLO materials, as well as $AgGaS_2$ (AGS),[14] $AgGaSe_2$ (AGSe)[15] and $ZnGeP_2$ (ZGP)[16] as middle- and far-infrared (MFIR) NLO materials. Consequently, the search for high-performance second-order NLO materials with balanced SHG properties, transparency range and laser-induced damage thresholds (LIDT) remains a challenge.

Due to the scarcity of nitrogen minerals in Earth's crust and challenging synthesis, nitrides remain relatively underexplored compared to their more abundantly available oxide counterparts.[17] However, owing to their unique electronic properties and robust bonding characteristics, nitrides have a wide range of applications, including optoelectronics, hard coatings and energy storage. As NLO materials, they also possess unique advantages, including (i) a wide band gap and high thermal conductivity, which may contribute to a high LIDT; (ii) outstanding chemical and thermal stability; and (iii) broad transparency windows spanning from the UV to the mid-IR region. In the late 20th century, both the linear and nonlinear optical responses of group-III nitrides have been extensively investigated through theoretical[18,19] and experimental[20,21] approaches. For instance, AlN and GaN films demonstrated relatively strong SHG responses, with d_{33} = 6.3 ± 3.5 pm/V@1064 nm[20] and d_{33} = 5.54 pm/V@1064 nm,[21] respectively. In

Received: January 14, 2025
Revised: April 20, 2025
Accepted: April 21, 2025
Published: May 7, 2025

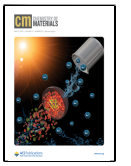

https://doi.org/10.1021/acs.chemmater.5c00109
Chem. Mater. 2025, 37, 3709−3719

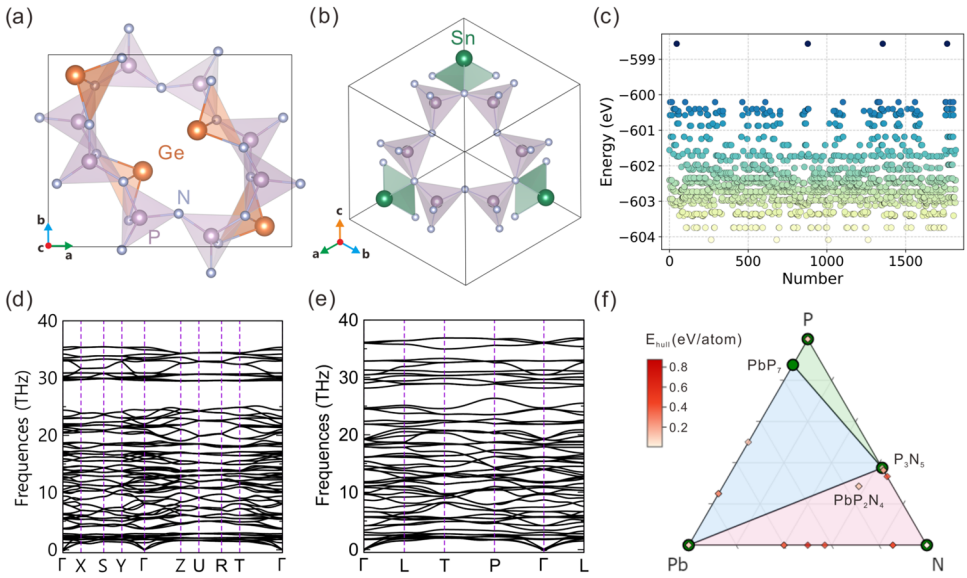

Figure 1. Primitive unit cells of (a) $Pna2_1$-GeP_2N_4 and (b) $R3m$-SnP_2N_4. (c) High-throughput screening of 1820 candidate SnP_2N_4 defect-free models using MACE large machine-learning model. Calculated phonon spectra for the predicted (d) $Pna2_1$- and (e) $R3m$-PbP_2N_4, respectively. (f) Ternary phase diagram of Pb−P−N system generated based on the Materials Project database.

recent years, NLO susceptibilities were characterized in TiN nanolayer,[22] defect h-BN flakes[23] and h-BN homostructures.[24] These findings suggest the potential for discovering efficient NLO materials among nitrides.

Based on theoretical calculations, several nitride compounds and nanosheets have been reported to possess an unprecedentedly strong SHG coefficient. Li et al.[25] predicted that the high-pressure synthesized $I\bar{4}2d$-$NaPN_2$ exhibits the highest SHG coefficient among phosphorus-based deep UV nonlinear optical materials, with a calculated static SHG coefficient d_{36} = 2.35 pm/V and a band gap of ∼6.2 eV. Furthermore, Zhang et al.[26] proposed a series of bulk and monolayer $ASnX$ (A = Na, H; X = N, P) compounds in which significant SHG effects were attributed to the polar divalent tin effect. For example, $P6_3mc$-NaSnN exhibits a large SHG coefficient d_{33} = 27 pm/V at static limit, accompanied by a band gap of ∼1.34 eV. Recently, Huang et al.[27] selected 34 asymmetric nitrides from the Inorganic Crystal Structure Database (ICSD),[28] and screened several nitrides possessing wide band gaps and large NLO coefficients. Among them, $Pmn2_1$-$MoZn_3N_4$ stands out with a notable NLO coefficient (d_{24} = − 16.70 pm/V in the static limit), a wide band gap of 3.05 eV and a high Debye temperature of 795.5 K, positioning it as a promising candidate for IR NLO applications. Additionally, utilizing an *ab initio* structural evolutionary algorithm method and high-throughput screening techniques, Pan's group[29,30] predicted and identified several nitrides with promising NLO and favorable thermal conductivity properties. For instance, $P3m1$-$ZrZnN_2$ was reported to have a large SHG response (d_{15} = 10.06 pm/V), a wide band gap of 3.11 eV and an *ab* plane thermal conductivity of 5.13 W/mK at 300 K. Collectively, these studies highlight the potential of nitrides as a critical system for the exploration of high-performance NLO materials.

Nitridophosphates,[31] a recently emerging subclass of nitrides, have attracted significant research interest due to their diverse structural variations, which originate from their fundamental building units—PN_4 tetrahedra. Experimentally, numerous NCS nitridophosphates have been reported, most of which are primarily composed of PN_4 tetrahedra. Representative examples include tetragonal MPN_2 (M = Cu, Li, Na),[32,33] orthorhombic TiP_4N_8,[34] hexagonal MP_2N_4 (M = Sr, Cd),[35] and cubic $A_3P_6N_{11}$(A = Na, K, Rb, Cs).[36] Additionally, some compounds exhibit less common PN_5 and PN_6 polyhedral units, such as MP_6N_{11} (M = Al, In)[37] and BP_3N_6,[38] respectively. Notably, some nitridophosphates featuring stereochemically active lone pairs (SCALPs) were recently reported, such as the sodalite-type $Sn_6[P_{12}N_{24}]$,[39] and the first germanium nitridophosphate GeP_2N_4,[40] in which Ge^{2+} exhibit unique SCALPs. Despite sharing identical stoichiometry, these two compounds adopt distinct structures, differentiating them from all other known MP_2N_4 systems (M = Be, Ca, Sr, Ba, Mn, Cd) due to the presence of SCALPs. Although the influence of SCALPs on structural and bonding properties has been highlighted,[40] the optical properties of these nitridophosphates remain unexplored, presenting an opportunity to investigate the NLO response of MP_2N_4 (M = Ge, Sn, Pb) family and explore the impact of SCALPs on the SHG property. Furthermore, the broader potential of nitridophosphates as a promising platform for NLO applications has yet to be fully realized.

Herein, based on state-of-the-art first-principles calculations coupled with a high-throughput screening technique, we identify MP_2N_4 (M = Ge, Sn, Pb) as the only known nitridophosphate family member exhibiting both pronounced SHG responses and sizable birefringence in the IR range. Our analysis utilizing atom response theory (ART) analysis[41−43] indicates that the SHG response of MP_2N_4 primarily arises from the nonbonding N 2p states, while the strong bonding states contribute minimally or even negatively. Additionally, we find that the charge density of SCALP near the Fermi level E_F is enhanced due to the stronger M-N s-p interactions. However, this enhancement does not necessarily correlate with an increased SHG response, as the overall contribution of SCALPs remains relatively minor. Moreover, we reveal two potential candidate compounds ($NaPN_2$ and HPN_2) with band gaps in the deep UV range, further highlighting nitridophosphates as a promising platform for the development of high-performance NLO materials.

https://doi.org/10.1021/acs.chemmater.5c00109
Chem. Mater. 2025, 37, 3709−3719

Table 1. Calculated $E_g^{PBE/LDA}$, E_g^{HSE}, Static d_{ij}, Static d_{eff}^p and Birefringence (Δn) at 1910 nm for $R3m$-and $Pna2_1$-MP_2N_4 (M = Ge, Sn, Pb)[f]

system	space group	$E_g^{PBE/LDA}$ (eV)	E_g^{HSE} (eV)	d_{ij}[a] (pm/V)	d_{eff}^p (pm/V)	Δn[a]	E_{hull}[e] (eV)
GeP_2N_4	$R3m$	3.47[a]	4.49[a]	$d_{15} = d_{24} = -3.438$[a]; $d_{31} = d_{32} = -3.138$[a]; $d_{22} = -d_{21} = -d_{16} = 2.898$[a]; $d_{33} = 2.103$[a];	3.967	0.046[a]	0.152
		3.38[b]		$d_{15} = d_{24} = -2.921$[b]; $d_{31} = d_{32} = -2.752$[b]; $d_{22} = -d_{21} = -d_{16} = 1.860$[b]; $d_{33} = 0.854$[b];	3.215	0.046[b]	
		3.37[c]		$d_{31} = d_{32} = d_{15} = d_{24} = -2.467$[c]; $d_{22} = -d_{21} = -d_{16} = 1.708$[c]; $d_{33} = 2.836$[c];	2.778		
	$Pna2_1$	3.20[a]	4.6 ± 0.2[d] 4.2 ± 0.4[d]	$d_{15} = -1.489$[a]; $d_{24} = -2.756$[a]; $d_{31} = -1.497$[a]; $d_{32} = -3.319$[a]; $d_{33} = 5.777$[a];	2.798	0.042[a]	0.167*
		4.2 ± 0.4[d]					
		3.17[b]		$d_{15} = -1.130$[b]; $d_{24} = -2.652$[b]; $d_{31} = -1.188$[b]; $d_{32} = -2.560$[b]; $d_{33} = 5.474$[b];	2.667	0.043[b]	
		3.13[c]		$d_{31} = -0.134$[c]; $d_{32} = -2.383$[c]; $d_{33} = 5.473$[c];	2.486		
		3.20[a]	4.27[a]	$d_{15} = -1.599$[a]; $d_{24} = -3.121$[a]; $d_{31} = -1.629$[a]; $d_{32} = -3.700$[a]; $d_{33} = 6.620$[a];	3.175	0.044[a]	
SnP_2N_4	$R3m$	3.09[a]	3.89[e] 3.96[a]	$d_{15} = d_{24} = -3.604$[a]; $d_{31} = d_{32} = -3.230$[a]; $d_{22} = -d_{21} = -d_{16} = 1.456$[a]; $d_{33} = 0.643$[a];	3.786	0.110[a]	0.074*
		2.97[b]		$d_{15} = d_{24} = -3.112$[b]; $d_{31} = d_{32} = -2.938$[b]; $d_{22} = -d_{21} = -d_{16} = -0.297$[b]; $d_{33} = -0.834$[b];	3.340	0.106[b]	
		2.97[c]		$d_{31} = d_{32} = d_{15} = d_{24} = -2.174$[c]; $d_{22} = -d_{21} = -d_{16} = -0.062$[c]; $d_{33} = 2.084$[c];	2.190		
	$Pna2_1$	2.68[a]	3.52[a]	$d_{15} = -1.301$[a]; $d_{24} = -3.221$[a]; $d_{31} = -1.405$[a]; $d_{32} = -3.918$[a]; $d_{33} = 9.727$[a];	4.118	0.112[a]	0.095
		2.61[b]		$d_{15} = -0.998$[b]; $d_{24} = -3.050$[b]; $d_{31} = -0.642$[b]; $d_{32} = -2.743$[b]; $d_{33} = 9.788$[b];	4.258	0.105[b]	
		2.64[c]		$d_{31} = -0.028$[c]; $d_{32} = -2.343$[c]; $d_{33} = 9.713$[c];	4.067		
PbP_2N_4	$R3m$	3.16[a]	3.94[e] 4.31[a]	$d_{15} = d_{24} = -5.071$[a]; $d_{31} = d_{32} = -4.206$[a]; $d_{22} = -d_{21} = -d_{16} = 0.779$[a]; $d_{33} = -1.601$[a];	5.408	0.084[a]	0.088
		3.08[b]		$d_{15} = d_{24} = -4.692$[b]; $d_{31} = d_{32} = -4.480$[b]; $d_{22} = -d_{21} = -d_{16} = 0.551$[b]; $d_{33} = -3.397$[b];	5.446	0.085[b]	
		2.97[c]		$d_{31} = d_{32} = d_{15} = d_{24} = -3.058$[c]; $d_{22} = -d_{21} = -d_{16} = 0.706$[c]; $d_{33} = 1.753$[c];	3.101		
PbP_2N_4	$Pna2_1$	2.86[a]	3.73[e] 4.07[a]	$d_{15} = -2.241$[a]; $d_{24} = -6.012$[a]; $d_{31} = -2.547$[a]; $d_{32} = -6.845$[a]; $d_{33} = 16.583$[a];	7.178	0.065[a]	0.098
		2.80[b]		$d_{15} = -1.757$[b]; $d_{24} = -5.704$[b]; $d_{31} = -1.829$[b]; $d_{32} = -6.046$[b]; $d_{33} = 17.219$[b];	7.376	0.067[b]	
		2.74[c]		$d_{31} = -1.455$[c]; $d_{32} = -5.684$[c]; $d_{33} = 14.650$[c];	6.509		

[a]Band gaps are calculated using VASP, d_{ij} and Δn are calculated based on SOS method using VASP + ARTATOP. [b]Calculated using SOS method as implemented in ABINIT. [c]Calculated within DFPT when applicable. [d]Experimentally measured band gaps from ref 40. In the scissor operator of $Pna2_1$-GeP_2N_4, the E_g^{EXP} = 4.6 is applied. [e]Calculated HSE + SOC band gap. [f]Compounds marked with * are experimentally observed.

2. RESULTS AND DISCUSSIONS

2.1. Crystal Structures and Electronic Structures. We first analyze the structure of the two experimentally synthesized SCALPs-containing MP_2N_4 compounds. GeP_2N_4 crystallizes in the NCS space group $Pna2_1$ (denoted as $Pna2_1$-GeP_2N_4) in which the P and N atoms each occupy two and four independent crystallographic positions, respectively, while the Ge atoms have one crystallographically unique site (Tables S1 and S2). All atoms are at special Wyckoff positions 2a. Each P atom forms distorted PN_4 tetrahedra with the four surrounding N atoms (N1, N2, N3, N4) with P−N bond lengths around 1.65 Å. The $P1N_4$ and $P2N_4$ tetrahedra alternate and share corners, resulting in the formation of a kinked eight-membered ring within the ab plane, characterized by a 4-up and 4-down configuration, which consequently creates a relatively large void along the c axis (Figure 1a). Besides, the P/N rings are corner-connected along the c axis, leading to an extended anion framework. Additionally, the Ge atoms are coordinated with three N atoms (N1, N2, N4), forming distorted GeN_3 pyramids with Ge−N bond lengths around 2.11 Å. Each GeN_3 pyramid is isolated, with the Ge atoms positioned at the apex of the pyramid, oriented toward the void. It is noteworthy that among the four types of N atoms, only N3 atoms are two-coordinated with two P atoms while all others are 3-fold-coordinated with one Ge atom and two P atoms, indicating that the N3 atoms are less covalently bonded than the other N atoms.

$Sn_6P_{12}N_{24}$ crystallizes in a sodalite-type structure with space group $I\bar{4}3m$, where the Sn atoms at the Wyckoff site 8c have a reduced occupation factor of 3/4 (Figure S1). Each set of six PN_4 tetrahedra forms a six-membered ring. All these rings are interconnected through edge-sharing tetrahedra, creating a cage-like framework. Sn atoms are positioned at the center of these six-membered rings, and are 3-fold coordinated in trigonal SnN_3 pyramids, where Sn lone pair points toward the central void of the cage. Due to the fractional occupancy, we performed a high-throughput screening of C_{16}^{12} = 1820 candidate models derived from the 2 × 1 × 1 superstructure of the experimental $Sn_6P_{12}N_{24}$ structure. The screening involved evaluating the energies of these structure models using predictions from the MACE large machine-learning model[44,45] (Figure 1c). A theoretical structure model in space group $R3m$ (denoted as $R3m$-SnP_2N_4, Figure 1b) was identified as the one with the lowest energy. It is worth noting that this model is not only energetically more stable by 3 meV/atom than the previously proposed theoretical $Cmm2$ model by Pucher et al.,[39] but also shows better agreement with the simulated X-ray diffraction (XRD) pattern of the experimental defect structure (Figure S1). In the $R3m$ structure, the PN_4 six-membered rings in the ab-

https://doi.org/10.1021/acs.chemmater.5c00109
Chem. Mater. 2025, 37, 3709−3719

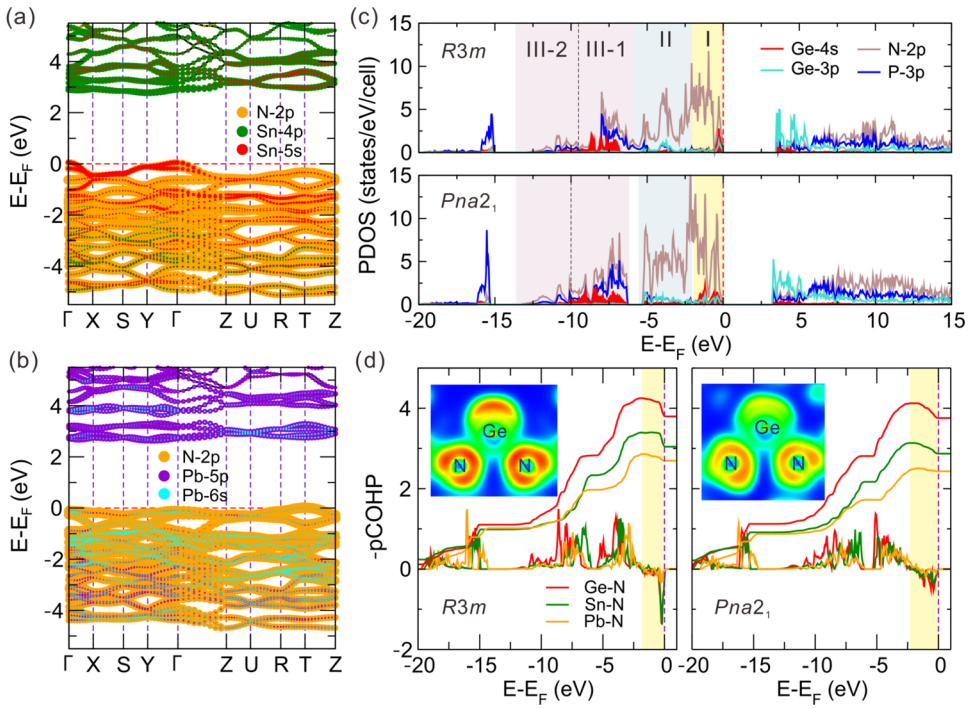

Figure 2. Fat band structures of (a) SnP_2N_4 and (b) PbP_2N_4 in $Pna2_1$ structure with SOC. (c) PDOS of $R3m$- and $Pna2_1$-GeP_2N_4. (d) Average -pCOHP and integrated COHP between M and N atoms for MP_2N_4. The inset figures are the 2D projection of the ELF for GeP_2N_4 showing the overall electronic localization around metal atoms.

plane do not have a central metal atom, leading to a layered structure in which every three Sn atoms form a regular triangle with a Sn−Sn distance of 3.65 Å. Sn and P atoms each occupy crystallographically unique sites while N atoms have three independent crystallographic positions, with only N2 atoms being 2-fold-coordinated with two P atoms.

Given that Ge^{2+}, Sn^{2+} and Pb^{2+} cations belong to the same periodic group, they can form SCALPs due to their ns^2 electron configuration. This makes it reasonable to design isostructural compounds in the MP_2N_4 family (M = Ge, Sn, Pb) based on the existing $Pna2_1$ and $R3m$ structure types. Besides, the ionic radii for Sn^{2+} (1.12 Å[46]) and Pb^{2+} (1.19 Å[47]) are comparable but significantly larger than that of Ge^{2+} (0.73 Å[47]), suggesting greater ionic polarizability. According to the semiempirical linear relationship between the effective SHG response d^p_{eff} and $\alpha_{sum}/(NE_g)$,[42,43,48] where α_{sum} represents the sum of the polarizabilities of all the ions in the primitive unit cell, N denotes the total number of atoms per primitive cell, and E_g is the band gap, a strong SHG response can be achieved by integrating highly polarizable atoms while maintaining a reduced band gap. This suggests that the SHG response can be enhanced by substituting smaller cations with larger, more polarizable counterparts under suitable chemical conditions. Consequently, isostructural MP_2N_4 compounds with larger metal cation polarizability are expected to exhibit stronger SHG responses.

The optimized crystal structure data for MP_2N_4 (M = Ge, Sn, Pb) in both $Pna2_1$ and $R3m$ structure types are summarized in Table S1. In terms of the total energy, the $R3m$ phases are energetically more favorable compared to the $Pna2_1$-MP_2N_4, with relative energies 0.015, 0.021, and 0.010 eV/atom lower for the Ge, Sn and Pb compounds, respectively. To further evaluate the stability of these MP_2N_4 phases, the energy above hull (E_{hull}) is calculated by generating the ternary phase diagrams (M−P-N), which also include the binary compounds, (M-P, M-N, and P−N systems) based on the Materials Project database.[49] E_{hull} measures the stability of a compound relative to decomposition into other stable phases. E_{hull} = 0 eV indicates a ground-state structure, while low positive values (<0.1−0.2 eV/atom) suggest metastability and potential synthesizability. As shown in Figures 1f and S2, MP_2N_4 is a metastable stoichiometry with E_{hull} values of 0.152, 0.074, and 0.088 eV/atom (Ge, Sn, Pb) in the $R3m$ phase, and 0.167, 0.095, and 0.098 eV/atom (Ge, Sn, Pb) in the $Pna2_1$ phase. Since $Pna2_1$-GeP_2N_4 and $R3m$-SnP_2N_4 have already been experimentally synthesized, other predicted compounds with similar E_{hull} values are also likely synthesizable under appropriate conditions. Furthermore, our phonon calculations indicate that all six MP_2N_4 compounds are dynamically stable, as evidenced by the absence of imaginary modes (Figures 1d,e and S3). According to the experimental findings,[39,40] the synthesis of $R3m$-MP_2N_4 may be feasible under ambient pressure conditions at high temperatures, while the synthesis of the $Pna2_1$ phases could potentially require high-pressure conditions. Thus, despite the significant difference in ionic radii between Sn^{2+} (1.12 Å) and Pb^{2+} (1.19 Å) compared to Ge^{2+} (0.73 Å), our calculations confirm that all four predicted structures remain thermodynamically and dynamically stable. This is further supported by the experimental synthesis of isostructural compounds containing Ge, Sn, and Pb, such as the monosulfides $Pnma$-MS (M = Ge, Sn, Pb),[49] demonstrating that such size variations do not prevent the formation of synthesizable, isostructural materials.

The SHG phenomenon of a material relates to how its electrons respond to an oscillating electric field E of light. Thus, it is crucial to identify the occupied and unoccupied states of these nitridophosphates that contribute to the excitations leading to the SHG response. Our calculated band structures (Figure S4) relying on the PBE exchange-correlation (XC) functional indicate an indirect band gap (E_g^{PBE}) of 3.20 eV from

https://doi.org/10.1021/acs.chemmater.5c00109
Chem. Mater. 2025, 37, 3709−3719

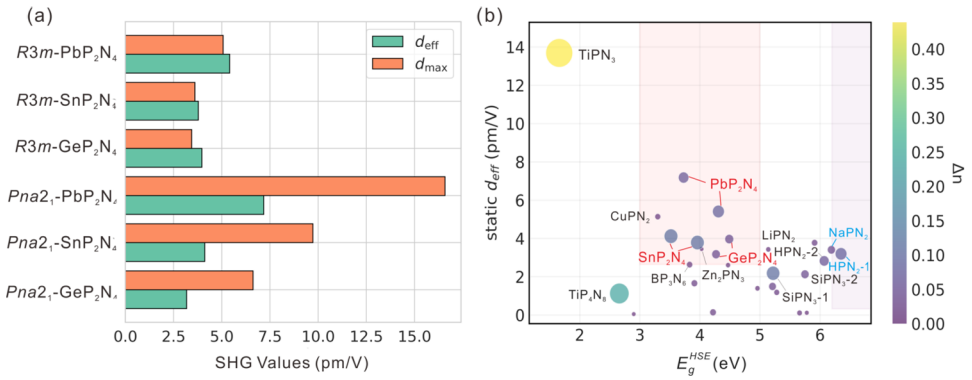

Figure 3. (a) Bar diagram for the d_{eff}^{p} and d_{max} value of *R*3*m*- and *Pna*2$_1$-MP_2N_4. (b) The distribution of E_g^{HSE} with respect to d_{eff}^{p} for 23 NCS nitridophosphates. The size and color of each point represent the value of Δ*n*. The red and purple shaded regions represent the elementary conditions for mid-IR NLO (3.0 eV < E_g < 5.0 eV and d_{eff}^{p} > 8 × KDP), and deep UV NLO (E_g > 6.2 eV and d_{eff}^{p} > 1 × KDP), respectively.

Γ to (0, 0, $k_z \approx 0.3214$) in *Pna*2$_1$-GeP_2N_4, which is smaller than the experimentally measured ones (E_g^{exp} = 4.6 ± 0.2, 4.2 ± 0.4 eV[40]). However, when the hybrid HSE XC functional is adopted, our calculated band gap (E_g^{HSE}) is 4.27 eV (Table 1), in good agreement with the experimental measurements. Compared to *Pna*2$_1$-GeP_2N_4, *Pna*2$_1$-SnP_2N_4 exhibit a significantly smaller band gap (E_g^{HSE} = 3.52 eV), which may be attributed to lattice expansion resulting from the larger ionic radius of Sn^{2+} substituting for Ge^{2+}. In contrast, *Pna*2$_1$-PbP_2N_4 lies between the two, with E_g^{HSE} = 4.07 eV. This trend remains consistent even when the spin−orbit coupling (SOC) effect is considered. As shown in Figures 2a,b and S4, the SOC effect leads to only a minor alteration in the valence bands (VBs) but induces slight band splitting in the conduction bands (CBs) in *Pna*2$_1$-SnP_2N_4, resulting in an overall unchanged band gap. However, SOC causes notable band splitting in both VBs and CBs in *Pna*2$_1$-PbP_2N_4, reducing the band gap by about 0.25 eV. Our subsequent calculations at the HSE+SOC level reveal a band gap of 3.73 eV for *Pna*2$_1$-PbP_2N_4 which remains larger than the E_g^{HSE} of SnP_2N_4 (Table 1). For *R*3*m*-MP_2N_4, the calculated indirect HSE band gaps are larger than those of the *Pna*2$_1$ phases, with an average increase of approximately 0.3 eV. Notably, *R*3*m*-PbP_2N_4 maintains an intermediate HSE band gap (E_g^{HSE} = 4.31 eV) among all three *R*3*m* phases, following the same order observed in the *Pna*2$_1$ phases. The inclusion of SOC results in a more pronounced reduction in the band gap (∼0.37 eV) in *R*3*m*-PbP_2N_4, rendering $E_g^{HSE+SOC}$ comparable to that of the Sn compound (Figure S5). The underlying reason for this ordering of the band gaps in MP_2N_4 will be discussed below. In terms of the band gap values, both structural families exhibit band gaps suitable for IR-range NLO applications.

To further understand the band gap trend in MP_2N_4, it is essential to analyze their electronic structures and bonding characteristics. As shown in Figures 2c and S6−S11, both *R*3*m* and *Pna*2$_1$-MP_2N_4 exhibit generally similar electronic structures. The upper portion of the VBs (region I, ∼ −2.3 eV to E_F) is primarily composed of nonbonding N 2p orbitals, with a minor contribution from hybridized *M* *n*s and *n*p states. It is noteworthy that weak *M*-N antibonding interactions are also detected at the top VBs. Relatively strong bonding interactions between N 2p and *M* *n*p states are observed in the energy range of −5.5 to −2.3 eV (region II). At deeper energies (−5.5 to −12.5 eV, region III), N 2p and P 3p states contribute nearly equally, with minor occupation of *M* *n*s orbitals, indicating the formation of strong N−P p−p covalent bonds and relatively weak *M*−N s−p interactions. Below −14.0 eV, the electronic states are dominated by strong N 3s-related P−N covalent bonding. Both the partial charge density (PCD) for the region I (Figure S12) and electron localization function (ELF) profiles (Figures 2d and S13), reveal highly asymmetric lobes located on the *M* atoms, indicative of the presence of SCALPs in MP_2N_4. However, the strength of SCALPs at the top VBs varies between the different structures and the *M* elements. From the -pCOHP and its integrated curves, the *M*-N bonding strength follows the order Ge > Sn > Pb in both *R*3*m* and *Pna*2$_1$-MP_2N_4, as does the antibonding interaction at top VBs. This suggests that SCALPs are pronounced in both GeP_2N_4 and SnP_2N_4, but weak in PbP_2N_4 in both structures. Specifically, the SCALPs on Ge can be visualized at an ELF value of 0.85, highlighting a significant degree of electron localization. From the COHP and ELF profile (Figures 2d and S13), PbP_2N_4 in both phases exhibits a substantially weakened covalent bonding interaction between Pb and N, accompanied by a marked increase in ionicity. Consequently, the top VBs in PbP_2N_4 are dominated by nearly pure nonbonding N 2p states, with negligible contributions from Pb 6s states or antibonding interactions. This phenomenon contrasts with the bonding characteristics found in GeP_2N_4 and SnP_2N_4. Thus, the absence of destabilizing antibonding interactions at the top VBs in PbP_2N_4 explains its larger band gap compared to SnP_2N_4, despite PbP_2N_4 having a larger volume and higher polarizability. Furthermore, COHP calculations reveal that both *M*−N bonding and antibonding interactions are stronger in the *R*3*m* phases than in *Pna*2$_1$, which is also evident in the 2D projected ELF maps (Figures 2d and S13), where electron localization is more pronounced in the *R*3*m* phases compared to *Pna*2$_1$. Additionally, the SCALPs in the *R*3*m* phases are mainly confined to a narrow energy range (∼0.55 eV) near E_F, whereas in the *Pna*2$_1$ phases, they are more dispersive (∼2.0 eV). This stronger covalent bonding interaction in the *R*3*m* phases contributes to their larger band gaps compared to the *Pna*2$_1$ phases. Furthermore, in the CBs, the lower portion primarily consists of *M*−N and P−N antibonding states, while the atomic orbitals, e.g., N 3p, P 3p and Ge 3d, overlap in the higher energy regions. Notably, the energy span of *M*−N antibonding states in *R*3*m* phases (E_g to 5.7 eV) is slightly broader than in *Pna*2$_1$ phases (E_g to 5.3 eV), consistent with the stronger *M*−N bonding interactions in the former.

2.2. Linear and Nonlinear Optical Properties. To compute optical properties, we apply the empirical scissor technique to PBE calculations, shifting the CB energies to match HSE or experimental band gaps where applicable. The SHG

https://doi.org/10.1021/acs.chemmater.5c00109
Chem. Mater. 2025, 37, 3709−3719

Table 2. Calculated E_g^{PBE}, E_g^{HSE}, Static d_{eff}^p and Birefringence (Δn) at 1910 nm for 23 NCS Nitridophosphates Documented in the Materials Project Database and ICSD[a]

ID[b]	system	N_{atom}	space group	E_g^{PBE} (eV)	E_g^{HSE} (eV)	d_{eff}^p (pm/V)	Δn	E_{hull}[c] (eV)
mp-989613	$TiPN_3$	5	$Amm2$	0.52	1.66	13.685	0.439	0.03
mp-1078469	$CuPN_2$	8	$I\bar{4}2d$	1.84	3.3	5.137	0.02	0.01*
ICSD-434261	$SrH_4P_6N_{12}$	23	$Fmm2$	4.43	5.91	3.773	0.023	*
mp-1102523	Zn_2PN_3	12	$Cmc2_1$	2.5	4.03	3.447	0.011	0*
mp-3524	$LiPN_2$	8	$I\bar{4}2d$	3.8	5.14	3.427	0.015	0*
mp-10572	$NaPN_2$	8	$I\bar{4}2d$	4.76	6.19	3.407	0.038	0*
mp-697139	HPN_2-1	16	$P2_12_12_1$	4.88	6.35	3.197	0.082	0*
mp-35220	HPN_2-2	8	$C2$[d]	4.67	6.07	2.827	0.057	<0.01
ICSD-20507	BP_3N_6	40	$Pna2_1$	2.48	3.83	2.633	0.022	*
ICSD-432590	$Li_{12}N_9P_3$	48	Cc	3.24	4.47	2.606	0.014	*
mp-36053	$SiPN_3$-2	20	Cc	3.73	5.22	2.183	0.106	0.02
mp-1219220	$SiPN_3$-1	10	$P2_1$	4.15	5.75	2.129	0.04	0.02
ICSD-147152	AlP_6N_{11}	18	Cm	2.36	3.91	1.66	0.025	*
ICSD-149735	LiP_4N_7	48	$P2_12_12_1$	3.72	5.21	1.494	0.034	*
mp-3933	Mg_2PN_3	12	$Cmc2_1$	3.56	4.96	1.395	0.015	0*
ICSD-175995	$SrSi_2PN_5$	36	$P2_12_12_1$	3.92	5.28	1.184	0.019	*
ICSD-46201	TiP_4N_8	26	$Pmn2_1$	1.32	2.66	1.126	0.226	*
mp-14712	Li_7PN_4	96	$P\bar{4}3n$	3.54	4.74	0.91	0	0*
mp-1196424	CdP_2N_4	168	$P6_3$[e]	2.79	4.22	0.142	0.025	0.01*
ICSD-425997	CaP_2N_4	168	$P6_3$	4.28	5.78	0.118	0.012	*
mp-645364	SrP_2N_4	168	$P6_3$	4.28	5.66	0.11	0.017	0*
mp-28161	$Na_3P_6N_{11}$	80	$P2_13$	4.04	5.4	0.096	0	0*
ICSD-147197	InP_6N_{11}	18	Cm	1.4	2.9	0.051	0.011	*

[a]The static d_{ij} for each compound are presented in Table S3. N_{atom} denotes the number of atoms in the primitive unit cell. [b]The prefix mp- and ICSD- denote the Materials Project database and ICSD database, respectively. [c]Available E_{hull} value from Materials Project database. Compounds marked with * are experimentally observed. [d]Relaxed structure of $I2_12_12_1$-HPN_2. [e]Relaxed structure of $P6_322$-CdP_2N_4.

properties and birefringence of $R3m$ and $Pna2_1$ MP_2N_4 are summarized in Table 1. For $Pna2_1$-MP_2N_4 ($mm2$ point group), the SHG tensor has five nonzero components, with three independent ones due to Kleinman symmetry: $d_{31} = d_{15}$, $d_{32} = d_{24}$ and d_{33}. In contrast, for the $R3m$ phase ($3m$ point group), intrinsic symmetry constraints result in eight nonzero components: d_{33}, $d_{22} = -d_{21} = -d_{16}$, $d_{31} = d_{32}$ and $d_{15} = d_{24}$, where the last two groups are related by Kleinman symmetry ($d_{31} = d_{32} = d_{15} = d_{24}$). However, when employing the "sum over states" (SOS) method, we observe that the Kleinman symmetry is not strictly respected in the static limit, i.e., $d_{31} \approx d_{15}$, $d_{32} \neq d_{24}$ (most probably due to small numerical errors). We do not to enforce Kleinman symmetry when employing the SOS method in this work. In contrast, the SHG tensor is also computed using density-functional perturbation theory (DFPT) for which Kleinman symmetry is inherently respected.[50,51] This approach yields quantitatively similar results to those obtained from the SOS method. It should be mentioned that the values calculated using SOS and DFPT are not supposed to be exactly the same. Indeed, the latter include the effect of the exchange-correlation kernel while the former do not. In the $Pna2_1$ phases, since d_{31} is not the dominant SHG component, this discrepancy does not lead to significant differences in the overall d_{eff}^p (an average SHG coefficient over all possible orientations of the powder crystals, estimated from the formula derived by Kurtz-Perry[52] and Cyvin et al.[53]). However, in the $R3m$ structure, the differences become larger, while the order of SHG remains. Therefore, this discrepancy, that does not play an important role in what follows, deserves further investigation, going, however, beyond the scope of the present work.

From the calculated largest SHG component and the effective d_{eff}^p, both the $R3m$ and $Pna2_1$ phases exhibit excellent NLO properties, as shown in Table 1 and Figure 3a. Specifically, the static d_{eff}^p of the experimentally synthesized $Pna2_1$-GeP_2N_4 and $R3m$-SnP_2N_4, calculated using both ARTATOP and ABINIT, are approximately 2.5−2.8 and 3.5−3.7 pm/V, which is about 8 and 11 times that of KDP (d_{eff}^{KDP} = 0.33 pm/V based on experimental d_{36}^{KDP}= 0.39 pm/V[54] at 1064 nm), respectively. Within the $Pna2_1$ phase, the largest SHG component d_{33} of GeP_2N_4 at static limit is ∼5.78 pm/V, which is about 14.82 times that of d_{36}^{KDP}. When Ge is substituted by Sn and Pb, the SHG response is further enhanced, with the d_{eff}^p increasing to 4.12 and 7.18 pm/V for $Pna2_1$-SnP_2N_4 and $Pna2_1$-PbP_2N_4, respectively. Notably, the largest d_{33} component of $Pna2_1$-PbP_2N_4 reaches 16.58 pm/V, surpassing that of AGS (d_{36} = 12.5 ± 2.5 pm/V[54]). Besides, it also possesses a much wider band gap ($E_g^{HSE+SOC}$ = 3.73 eV) compared to AGS (2.64 eV[54]), indicating that $Pna2_1$-PbP_2N_4 may exhibit superior overall performance as an IR NLO material. Comparing the $Pna2_1$ and $R3m$ phases, the largest SHG component of the $Pna2_1$ compounds are significantly higher, approximately 1.7−3.8 times those of the $R3m$ phases. The effective d_{eff}^p values of $Pna2_1$ are also generally stronger. Interestingly, $R3m$-GeP_2N_4 shows a slightly larger d_{eff}^p compared to the $Pna2_1$ phase, despite having a relatively smaller largest SHG component (d_{15}). This is because d_{eff}^p is a weighted average of the squares of multiple d_{ij} components, and if each d_{ij} component is relatively large, the d_{eff}^p value may exceed the largest individual d_{ij} component. Additionally, the enhancement effect induced by metal substitution in the $Pna2_1$ compounds is more pronounced compared to the $R3m$ counterparts. The relevant mechanism and the origin of SHG will be discussed below.

Our calculations of the refractive indices as a function of wavelength (Figure S14) reveal that both the experimentally

https://doi.org/10.1021/acs.chemmater.5c00109
Chem. Mater. 2025, 37, 3709−3719

synthesized $Pna2_1$-GeP_2N_4 and $R3m$-SnP_2N_4 can achieve Type-I phase-matching ($n^{\omega} = n^{2\omega}$) behavior when the fundamental wavelengths exceed 1.22 and 0.82 μm, respectively, falling within the infrared range. Furthermore, these two materials satisfy the Type-II phase-matching condition at fundamental wavelengths of 1.68 and 1.22 μm, respectively. Furthermore, the calculated birefringence value Δn for $Pna2_1$-GeP_2N_4 is 0.044 at 1910 nm (Table 1), which falls within the range suitable for technical applications (ca. 0.03−0.10). The results indicate that GeP_2N_4 is a promising candidate for applications in the IR range as a NLO material. Furthermore, $R3m$-SnP_2N_4 displays a remarkable birefringence of 0.112 at 1910 nm and a short cutoff edge at ∼314 nm (3.96 eV), suggesting its potential as an excellent candidate birefringent material (i.e., with a birefringence ≥0.1 and a cutoff edge <420 nm).[55]

2.3. Prediction and Screening of NLO Nitridophosphates. We extend our search further by first identifying 67 nitridophosphates in the Materials Project database, excluding those containing other anions such as O^{2-}, S^{2-}, F^-, Cl^-, and Br^-, as well as organic−inorganic hybrid compounds. Additionally, we screen another 160 entries in the Inorganic Crystal Structure Database (ICSD)[28] to supplement our data set with recently synthesized compounds. We then apply a few initial screening criteria—specifically, having a NCS structure, a value of E_g^{PBE} greater than 0, a nonmagnetic nature, and a primitive cell with less than 170 atoms—to narrow our selection to 26 nitridophosphates for subsequent calculations. The calculated E_g^{HSE}, static d_{eff}^p, and birefringence at 1910 nm for 23 nitridophosphates with nonzero SHG response are presented in Figure 3b, and in Tables 2 and S3. Note that, 3 compounds with vanishing SHG tensor are omitted due to intrinsic symmetry (see Table S3 for detail). It can be observed that, compared to the 23 NCS nitridophosphates, only the MP_2N_4 family compounds exhibit significant SHG responses with sizable birefringence, all within the band gap range considered appropriate for IR NLO materials. Figure 3b further highlights that $I\bar{4}2d$-$CuPN_2$, $Cmc2_1$-Zn_2PN_3 and $Pna2_1$-BP_3N_6 exhibit large SHG response in the IR range, with effective d_{eff}^p of 5.14, 3.44, and 2.63 pm/V, respectively. However, their birefringence values remain relatively low (<0.022), which might limit their practical applications. Furthermore, in the band gap range exceeding 5 eV, $P2_12_12_1$-HPN_2 (HPN_2-1) exhibits the deepest UV cutoff edge with a E_g^{HSE} of 6.35 eV, a strong SHG response (static d_{eff}^p = 3.20 pm/V, ∼9.7 × KDP) and a shortest Type I phase-matching wavelength of 296.4 nm (second-harmonic wavelength), making it a promising candidate for UV NLO applications. Similarly, $I\bar{4}2d$-$NaPN_2$ holds a high E_g^{HSE} of 6.19 eV, the largest SHG response (static d_{eff}^p = 3.41 pm/V, ∼10.3 × KDP) and a sizable birefringence (0.038 at 1910 nm). Note that our calculated results for $I\bar{4}2d$-$NaPN_2$ agree well with the findings of Li et al.,[25] who also observed such very large bandgap by MBJLDA. However, its shortest phase-matching second-harmonic wavelength of 451.4 nm places it outside the UV or deep-UV range, making it more suitable for visible NLO applications (Figure S15). Additionally, within this deep wavelength range, Cc- and $P2_1$-$SiPN_3$, and $C2$-HPN_3 are predicted to exhibit strong SHG response and suitable birefringence. Among all the nitridophosphates investigated, $Amm2$-$TiPN_3$ has the highest SHG response (static d_{eff}^p of 13.69 pm/V) and birefringence (0.49 at 1910 nm), despite its relatively low band gap (∼1.66 eV). Note that, the available E_{hull} values for these NCS nitridophosphates listed in Table 2 are all relatively low, suggesting a high probability of experimental synthesizability for these NCS nitridophosphates. In fact, the compounds marked with an * have already been experimentally synthesized, further emphasizing the potential of nitridophosphates as a promising platform for the development of advanced NLO materials.

2.4. The Role of SCALPs in the SHG Response. *2.4.1. Partial Response Function Analysis.* Such findings naturally call for a better understanding of the underlying mechanisms for the SHG response of MP_2N_4 (M = Ge, Sn, Pb). By employing the partial response function (PRF) and ART analysis,[41−43] insights into the origins of the SHG response at both the atomic and orbital levels can be obtained. Figures S6c−S11c show the PRFs, $\zeta_V(E_B)$ and $\zeta_C(E_B)$ for the largest SHG component of $R3m$ and $Pna2_1$-MP_2N_4. We start from the $Pna2_1$ phases with larger SHG response. For $Pna2_1$-GeP_2N_4, a sharp increase in the $\zeta_V(E_B)$ function is observed in region I, where the nonbonding N 2p states and the SCALPs of Ge dominate, while it decreases dramatically in region II where the Ge−N p−p bonding states occur (Figure S9c). This observation suggests that the nonbonding states at the top VBs contribute significantly and positively to the SHG response, whereas the bonding states exert a negative influence. It is noteworthy that the SCALPs-related states of Ge^{2+} are divided into two distinct regions. The first region, located at the top of the VBs, comprises 16 bands within region I (mainly in the top 8 bands, see Figure S16), which exhibit pronounced stereochemical activity, as depicted in the projected PCD in Figure 4a. The second region,

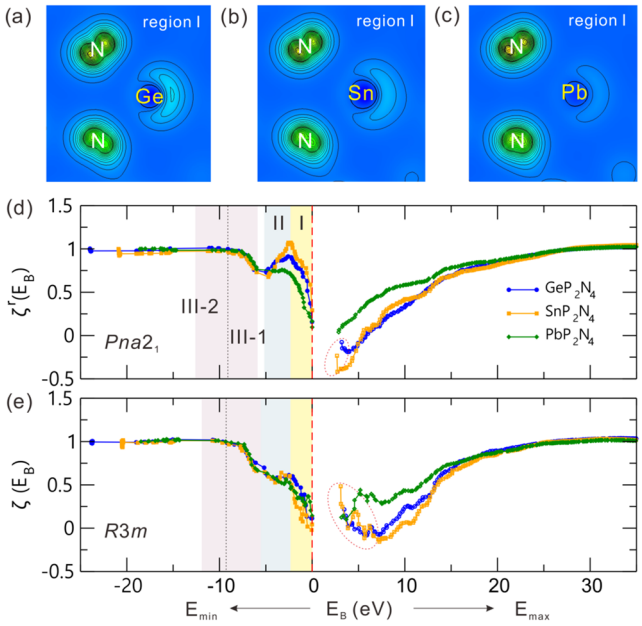

Figure 4. 2D projection of partial charge density (PCD) for (a−c) region I (top 16 bands in VBs) for $Pna2_1$-MP_2N_4, illustrating the nonbonding electrons on N atoms and SCALPs on M^{2+} ions. Relative PRF curve for the largest SHG component (d) d_{33} of $Pna2_1$-MP_2N_4 and (e) $R3m$-MP_2N_4.

located at a relatively deeper energy level, also contains 16 bands in region III-1 and displays a nearly spherical configuration, contributing to weak bonding interactions with the N 2p states (Figure S17). Furthermore, the SCALPs of Ge^{2+} in both energy ranges do not purely consist of s orbitals but rather of Ge sp hybrid orbitals. Interestingly, in region III, where the Ge−N s−p interactions and N−P p−p covalent bonding interactions occur,

https://doi.org/10.1021/acs.chemmater.5c00109
Chem. Mater. 2025, 37, 3709−3719

the $\zeta_V(E_B)$ function exhibits an upward trend once more (Figure S9c). Although the Ge−N and N−P bonding interactions span a broad energy range from −13 to −7 eV, noticeable changes in the $\zeta_V(E_B)$ function are only observed within region III-1, where the Ge 4s states are situated. In contrast, region III-2, dominated by almost pure P−N covalent bonding, shows minimal changes in the $\zeta_V(E_B)$ function. This observation implies that the highly polarizable SCALPs-related states, are primarily responsible for the variations in the PRF within region III rather than the tightly bonded P−N states. As further evidence, the $\zeta_V(E_B)$ function changes little in the deep energy regions below 8 eV where various types of strong covalent bonding states dominate. Regarding the CBs, within a narrow energy range from CBM to 4.8 eV, the $\zeta_C(E_B)$ function experiences a slight decrease with increasing E_B, indicating a subtle negative contribution from Ge−N p−p antibonding states. However, the $\zeta_C(E_B)$ function rises steadily at the higher energy levels, where the P−N antibonding and unoccupied atomic orbitals are located, reflecting the strong positive contribution from these unoccupied states. Therefore, the orbitals contributing positively to the SHG are primarily the nonbonding N 2p states, along with the SCALPs-related states at VBs in $Pna2_1$-GeP_2N_4, while the bonding states show minor contributions.

To analyze the similarities and differences of the SHG origin within the $Pna2_1$-MP_2N_4 compounds, each PRF is rescaled as $\zeta_V(E_B)/\zeta_T$ and $\zeta_C(E_B)/\zeta_T$, where $\zeta_T = \zeta_V(E_{min}) = \zeta_C(E_{max})$ denotes the value of the total response contributed by all VBs and CBs of a specific compound. This approach is referred to as the relative PRF (RPRF), which normalizes the PRF at both lower and upper energy bounds. As illustrated in Figure 4d, the primary features of $\zeta^r_V(E_B)$ and $\zeta^r_C(E_B)$ in both regions I and III are similar for the three compounds, showing significant positive contributions. However, a notable distinction is the absence of a strong negative contribution in region II for $Pna2_1$-PbP_2N_4, which is present in both SnP_2N_4 and GeP_2N_4. This leads to two important insights. First, the nonbonding N 2p and SCALPs-related states, including both the *M* sp hybrid states at the top VBs (region I) and deeper VBs (region III-1), serve as a common origin of SHG in the MP_2N_4 compounds. In contrast, the *M*-N p−p bonding interactions in region II either contribute minimally or exert a negative effect on SHG. Second, the quantity of SCALPs in region I follows the order PbP_2N_4 < SnP_2N_4 < GeP_2N_4, as evidenced by the PCD (Figure 4a−c) and ELF (Figures 2d and S13), which is completely contradictory to the calculated order of SHG responses, indicating that the strength of SCALPs in $Pna2_1$-MP_2N_4 does not have a direct correlation with the overall SHG properties. Furthermore, the formation of strong SCALPs in region I and III-1 also leads to a negative contribution in region II. In materials with strong SCALPs, such as GeP_2N_4 and SnP_2N_4, the asymmetric orbitals at the top VBs are highly oriented and polarizable. This characteristic can result in a response to the electric field of light that is opposite in sign compared to the energetically lower bonding region. However, in $Pna2_1$-PbP_2N_4, where the SCALPs are relatively weak, the negative contribution in region II is less pronounced than in its Ge and Sn counterparts. This suggests that the SHG response is intricately linked to the nature of bonding.

The significantly enhanced SHG response in $Pna2_1$-PbP_2N_4 can be attributed to the increased ionic character of the Pb−N bond and the overall ionic polarizability of the material. The substantial reduction in covalent interaction between Pb and N leads to a marked decrease in the asymmetric SCALPs on Pb atoms. As a result, the orbitals oscillating in response to the electric field do not exhibit pronounced polarization directionality, thereby avoiding the opposite response associated with covalent bonding states. Consequently, no significant negative contributions are detected in region II of $Pna2_1$-PbP_2N_4, unlike in the Ge and Sn compounds (Figure 4d). Despite the considerable contributions from nonbonding N 2p and Pb 6s states in the VB, the unoccupied Pb 5p states in CBs also play a significant role in the SHG response, as shown in Table S4. This analysis elucidates the reasons behind $Pna2_1$-PbP_2N_4 exhibiting the highest SHG response among the three isostructural compounds.

For $R3m$-MP_2N_4, the RPRFs $\zeta^r_V(E_B)$ exhibit overall similar features (Figure 4e), indicating significant positive contributions from both regions I and III−I, while contributions from region II remain minor. These findings suggest that the nonbonding N 2p states and SCALP-related states serve as the primary origin of the SHG response, whereas bonding states play a comparatively minor role. This trend is generally consistent with that observed in the $Pna2_1$ phases. However, in $R3m$-GeP_2N_4 and $R3m$-SnP_2N_4 where the SCALPs are primarily concentrated in the top two bands within a narrow energy range (∼0.55 eV), the $\zeta^r_V(E_B)$ function of $R3m$-GeP_2N_4 remains nearly unchanged, whereas in $R3m$-SnP_2N_4, it exhibits a downward shift, suggesting weak or even negative contributions from SCALPs (Figures 4e and S6−S7). In contrast, in $R3m$-PbP_2N_4 where the SCALPs associated with Pb are weak, $\zeta^r_V(E_B)$ increase steadily (Figures 4e and S8c). This suggests that when SCALPs are either excessively strong or highly localized, they may fail to synergize with the nonbonding states from anions, potentially leading to contributions that counteract those of the nonbonding states. Furthermore, the negative contributions from antibonding states in the lower part of the conduction bands are more pronounced in the $R3m$ phases. For the Ge and Sn compounds, $\zeta^r_C(E_B)$ exhibits a clear negative trend over a broad energy range (∼4 eV), whereas a positive trend is observed for the Pb compound. This further supports the conclusion that strong chemical interactions do not favor the SHG response. However, such strong negative contributions are nearly absent in the $Pna2_1$ phases, where the SCALPs are more evenly distributed in region I, and the *M*−N antibonding interactions are relatively weak. Due to the significant negative contributions associated with strong *M*−N interactions in the $R3m$ phases, these structures exhibit a relatively lower SHG response compared to their $Pna2_1$ counterparts.

2.4.2. Individual Atom Contributions. The quantitative contribution A_τ (in %) of an individual atom τ to the strongest SHG coefficient d_{33} for $Pna2_1$-MP_2N_4 and d_{15} for $R3m$-MP_2N_4 are obtained based on the PRFs. As presented in Table S4, for all three compounds in the $Pna2_1$ structure, the A_τ of the metal element *M* is the highest (∼5.55%), surpassing that of the N atoms (∼3.68%), while P atoms exhibit the lowest A_τ values (∼2.36%). Considering the number of atoms of each type in the unit cell, the total contributions of the elements are ranked as follows: N (60.49%) ≫ *M* (21.24%) > P (18.27%). The significant contribution of the N atoms is primarily attributed to the occupied nonbonding N 2p states. In both $Pna2_1$-GeP_2N_4 and $Pna2_1$-SnP_2N_4, the metal *M ns* states in the VB and the *M nd* states in the CB contribute strongly, with the contribution from the VB being larger than that from the CB. This is an unusual phenomenon for metal atoms and is attributed to the presence of SCALPs, which enhance the contribution of the VB. However, in $Pna2_1$-PbP_2N_4, the SCALPs are relatively weak, leading to a

https://doi.org/10.1021/acs.chemmater.5c00109
Chem. Mater. 2025, 37, 3709−3719

reduced contribution from the Pb 6s states, while the contribution from the 5p states in the CB increases. This behavior is characteristic of metals with larger atomic radii, such as Ba in BBO, Cs in CBO, and Sr in SBBO,[43,56] etc. For the $R3m$-MP_2N_4 phase, the largest contribution to the total SHG response originates from the N atoms, accounting for 69.4, 86.3, and 57.7% in the Ge, Sn, and Pb compounds, respectively. However, regarding the metal contributions, significant negative contributions are observed for Ge and Sn, particularly from their s and p orbitals in the CBs. This aligns with the negative change in $\zeta^{\tau}_{C}(E_B)$ (Figure 4e), leading to a reduction in the overall metal contribution to SHG. In contrast, Pb atoms exhibit strong positive contributions, with A_τ (7.64%) being 1.6 times that of N atoms, which primarily originate from the Pb 6s states in the VB and the 5p and 5d states in the CB.

Furthermore, according to ART, the quantitative total contribution of the SCALPs-related states in regions I and III for $Pna2_1$-GeP_2N_4, SnP_2N_4 and PbP_2N_4 are 13.04, 18.56, and 6.29%, respectively. These contributions account for only approximately 30% of the contributions from the nonbonding N 2p states (41.78, 47.94, and 33.57%, respectively). In the $R3m$ phase, the total contribution of SCALPs-related states in regions I and III is even lower, at 6.95, 2.39, and 7.36% for Ge, Sn, and Pb compounds, respectively. This finding suggests that although SCALPs do contribute positively to SHG in MP_2N_4, they are not the primary source, and a higher strength of SCALPs does not necessarily correlate with a stronger SHG response.

3. CONCLUSIONS

In summary, our first-principles computations reveal that MP_2N_4 (M = Ge, Sn, Pb) compounds, in both $Pna2_1$ and $R3m$ structures, stand out as promising candidates for IR NLO applications, characterized by remarkable band gaps, strong SHG response and sizable birefringence among all known NCS nitridophosphates. Specifically, the recently experimental synthesized $Pna2_1$-GeP_2N_4 and $R3m$-SnP_2N_4 exhibits a wide band gap (4.6 and 3.96 eV, respectively), large static d^{p}_{eff} (2.79 and 3.78 pm/V) and sizable birefringence (0.044 and 0.011 at 1910 nm), with both Type I and Type II phase-matching behavior. Moreover, the predicted compound $Pna2_1$-PbP_2N_4 exhibits a superior effective SHG response of 7.18 pm/V (~21.7 × KDP) and the largest SHG component d_{33} = 16.58 pm/V (~1.32 × d^{AGS}_{36}) at static limit, alongside a large band gap ~3.73 eV. Electronic structure calculations incorporating SOC reveal an unexpected ordering of the band gaps of these three compounds (Ge > Pb > Sn). The significantly reduced antibonding interactions (SCALPs) at the top VBs for PbP_2N_4 are identified as the factor responsible for its enhanced band gap. Further analyses based on ART and PRF indicate that the predominant contributor to the SHG is the nonbonding N 2p states at VB, while the bonding states contribute minimally or negatively. Moreover, the order of SHG response is inversely related to the strength of SCALPs at the top VBs, suggesting that the latter are not the primary contributors to the SHG response in MP_2N_4 family in both $Pna2_1$ and $R3m$ structures. Notably, in the more ionic PbP_2N_4, the unoccupied 5p states play a significant role in determining its large SHG response, highlighting the important contribution of conduction bands from large metal atoms. Additionally, we reveal 23 NCS nitridophosphates with nonzero second-harmonic generation (SHG) responses through high-throughput screening of nitridophosphate compounds in the ICSD and Materials Project database. Among them, $TiPN_3$ has the highest SHG response (static d^{p}_{eff} = 13.69 pm/V) and birefringence (0.49 at 1910 nm), though its band gap is relatively low. In contrast, $NaPN_2$ and HPN_2 exhibit impressive SHG response (~10 × KDP) combined with remarkable band gaps exceeding 6.2 eV, making them promising candidates for UV and visible NLO applications. These findings not only enhance our understanding of the relationship between electronic structure and nonlinear optical properties in nitridophosphates but also demonstrate the potential of nitridophosphates as a promising platform for designing next-generation NLO materials.

4. METHODS

The crystal structures of the MP_2N_4 compounds and other NCS nitridophosphates from the ICSD and the Materials Project database are optimized by density functional theory (DFT) calculations using the Perdew−Burke−Ernzerhof (PBE) exchange-correlation functional[57] encoded in the Vienna *ab initio* simulation package (VASP).[58−60] These optimized structures are used for our optical property calculations using the sum over states (SOS) method[18,61−64] as well as the DFPT framework. Since standard DFT calculations underestimate the band gaps, we use a scissor operator[50] to raise the energies of the unoccupied states to match either the experimental band gaps or the theoretical ones as computed by the hybrid functional HSE06.[65] To check the dynamical stability, we further calculated the phonon dispersion curves using the finite-displacement approach as implemented in the Phonopy code.[66] In our calculations for the SHG responses, we employed the SOS method using the code (ARTATOP) that was developed[41] on the basis of the calculated electronic structures obtained from the VASP code. For MP_2N_4, the SHG properties are further verified using ABINIT,[51,67,68] both via SOS and DFPT. To determine the contributions of specific atomic orbital states, and hence the relative contributions of the individual atoms, to the SHG coefficients, we introduce the PRF for the SHG coefficients associated with the valence bands (VBs) and the conduction bands (CBs). For each of the MP_2N_4 compounds, the contributions A_τ of the individual atoms τ to a specific component (e.g., the largest one) of the total SHG response tensor were determined by performing the ART analyses[41−43] (for detailed computational methods, see the Supporting Information).

■ ASSOCIATED CONTENT

Supporting Information

The Supporting Information is available free of charge at https://pubs.acs.org/doi/10.1021/acs.chemmater.5c00109.

Computational details; Optimized crystal structure data; Electronic structures; Ternary phase diagram, PCD and ELF profiles; PRF and ART analysis (PDF)

■ AUTHOR INFORMATION

Corresponding Authors

Xiyue Cheng − *State Key Laboratory of Structural Chemistry, Fujian Institute of Research on the Structure of Matter, Chinese Academy of Sciences, Fuzhou 350002 Fujian, P. R. China; Key Laboratory of Optoelectronic Materials Chemistry and Physics, Fujian Institute of Research on the Structure of Matter, Chinese Academy of Sciences, Fuzhou 350108 Fujian, P. R. China; Institute of Condensed Matter and Nanosciences, UCLouvain, B-1348 Louvain-la-Neuve, Belgium;* orcid.org/0000-0003-2440-394X; Email: xycheng@fjirsm.ac.cn

Shuiquan Deng − *State Key Laboratory of Structural Chemistry, Fujian Institute of Research on the Structure of Matter, Chinese Academy of Sciences, Fuzhou 350002 Fujian, P. R. China; Key Laboratory of Optoelectronic Materials Chemistry and Physics, Fujian Institute of Research on the Structure of Matter, Chinese Academy of Sciences, Fuzhou*

https://doi.org/10.1021/acs.chemmater.5c00109
Chem. Mater. 2025, 37, 3709−3719

350108 Fujian, P. R. China; orcid.org/0000-0001-5538-6738; Email: sdeng@fjirsm.ac.cn

Authors

Victor Trinquet − *Institute of Condensed Matter and Nanosciences, UCLouvain, B-1348 Louvain-la-Neuve, Belgium*

Bohan Ding − *State Key Laboratory of Structural Chemistry, Fujian Institute of Research on the Structure of Matter, Chinese Academy of Sciences, Fuzhou 350002 Fujian, P. R. China*

Gian-Marco Rignanese − *Institute of Condensed Matter and Nanosciences, UCLouvain, B-1348 Louvain-la-Neuve, Belgium;* orcid.org/0000-0002-1422-1205

Xavier Gonze − *Institute of Condensed Matter and Nanosciences, UCLouvain, B-1348 Louvain-la-Neuve, Belgium;* orcid.org/0000-0002-8377-6829

Complete contact information is available at: https://pubs.acs.org/10.1021/acs.chemmater.5c00109

Author Contributions

X.C. and S.D. conceived the project. X.C. and V.T. carried out the DFT calculations. X.C., V.T., B.D., G.-M.R., and X.G. contributed to data analysis. X.C. wrote the drafts. X.C., V.T., B.D., G.-M.R., X.G., and S.D. revised the manuscript. All authors discussed the results and provided comments during the manuscript preparation.

Notes

The authors declare no competing financial interest.

■ ACKNOWLEDGMENTS

This work was financially supported by the National Natural Science Foundation (NSF) of China (22031009, 21921001, 22075282, 62475265); the National Key R&D Program of China (2021YFB3601501); the NSF of Fujian Province (2023J01212). Computational resources have been provided by the supercomputing facilities of National Supercomputer Center in Tianjin and the Université catholique de Louvain (CISM/UCL) and the Consortium des Équipements de Calcul Intensif en Fédération Wallonie Bruxelles (CÉCI) funded by the Fond de la Recherche Scientifique de Belgique (F.R.S.-FNRS) under convention 2.5020.11 and by the Walloon Region. The present research benefited from computational resources made available on Lucia, the Tier-1 supercomputer of the Walloon Region, infrastructure funded by the Walloon Region under the grant agreement n°1910247. V.T. acknowledges the support from the FRS-FNRS through a FRIA Grant.

■ REFERENCES

(1) Shen, Y. R. *The Principles of Nonlinear Optics*; Wiley-Interscience, 1984.

(2) Boyd, R. W. *Nonlinear Optics*; Elsevier, 2003.

(3) Ok, K. M. Toward the rational design of novel noncentrosymmetric materials: factors influencing the framework structures. *Acc. Chem. Res.* **2016**, *49* (12), 2774−2785.

(4) Wang, W.; Mei, D.; Liang, F.; Zhao, J.; Wu, Y.; Lin, Z. Inherent laws between tetrahedral arrangement pattern and optical performance in tetrahedron-based mid-infrared nonlinear optical materials. *Coord. Chem. Rev.* **2020**, *421*, No. 213444.

(5) Chen, J.; Hu, C. L.; Kong, F.; Mao, J. G. High-performance second-harmonic-generation (SHG) materials: new developments and new strategies. *Acc. Chem. Res.* **2021**, *54* (12), 2775−2783.

(6) Cheng, M.; Hou, X.; Yang, Z.; Pan, S. Recent progress in borate-based short-wavelength nonlinear optical crystals with boron−oxygen skeleton modification. *Mater. Chem. Front.* **2023**, *7* (20), 4683−4692.

(7) Tran, T. T.; Yu, H.; Rondinelli, J. M.; Poeppelmeier, K. R.; Halasyamani, P. S. Deep ultraviolet nonlinear optical materials. *Chem. Mater.* **2016**, *28* (15), 5238−5258.

(8) Liu, Y.; Shen, Y.; Zhao, S.; Luo, J. Structure-property relationship in nonlinear optical materials with π-conjugated CO3 triangles. *Coord. Chem. Rev.* **2020**, *407*, No. 213152.

(9) Chen, H.; Wei, W.-B.; Lin, H.; Wu, X.-T. Transition-metal-based chalcogenides: A rich source of infrared nonlinear optical materials. *Coord. Chem. Rev.* **2021**, *448*, No. 214154.

(10) Zhao, X.; Lin, C.; Tian, H.; Wang, C.; Ye, N.; Luo, M. Nitrides: a promising class of nonlinear optical material candidates. *Mater. Chem. Front.* **2023**, *7* (22), 5744−5759.

(11) He, J.; Guan, Y.; Trinquet, V.; Brunin, G.; Wang, K.; Robinson, R.; Zu, R.; Yoshida, S.; Lee, S. H.; Wang, Y.; et al. $MgSiP_2$: an infrared nonlinear optical crystal with a large non-resonant phase-matchable second harmonic coefficient and high laser damage threshold. *Adv. Opt. Mater.* **2023**, *11* (24), No. 2301060.

(12) Chen, C. T.; Wu, B. C.; Jiang, A. D.; You, G. M. A new-type ultraviolet SHG crystal-β-BaB_2O_4. *Sci. Sin., Ser. B* **1985**, *28* (3), 235−243.

(13) Chen, C. T.; Wu, Y. C.; Jiang, A. D.; Wu, B. C.; You, G. M.; Li, R. K.; Lin, S. J. New nonlinear-optical crystal: LiB_3O_5. *J. Opt. Soc. Am. B* **1989**, *6*, 616−621.

(14) Abrahams, S. C.; Bernstein, J. L. Crystal structure of piezoelectric nonlinear-optic $AgGaS_2$. *J. Chem. Phys.* **1973**, *59* (4), 1625−1629.

(15) Boyd, G.; Kasper, H.; McFee, J.; Storz, F. Linear and nonlinear optical properties of some ternary selenides. *IEEE J. Quantum Electron.* **1972**, *8* (12), 900−908.

(16) Mason, P. D.; Jackson, D. J.; Gorton, E. K. CO_2 laser frequency doubling in $ZnGeP_2$. *Opt. Commun.* **1994**, *110* (1−2), 163−166.

(17) Gagné, O. C. On the crystal chemistry of inorganic nitrides: crystal-chemical parameters, bonding behavior, and opportunities in the exploration of their compositional space. *Chem. Sci.* **2021**, *12* (12), 4599−4622.

(18) Rashkeev, S. N.; Lambrecht, W. R.; Segall, B. Efficient *ab initio* method for the calculation of frequency-dependent second-order optical response in semiconductors. *Phys. Rev. B* **1998**, *57* (7), No. 3905.

(19) Gavrilenko, V. I.; Wu, R. Q. Linear and nonlinear optical properties of group-III nitrides. *Phys. Rev. B* **2000**, *61* (4), No. 2632.

(20) Fujii, Y.; Yoshida, S.; Misawa, S.; Maekawa, S.; Sakudo, T. Nonlinear optical susceptibilities of AlN film. *Appl. Phys. Lett.* **1977**, *31* (12), 815−816.

(21) Miragliotta, J.; Wickenden, D.; Kistenmacher, T.; Bryden, W. Linear-and nonlinear-optical properties of GaN thin films. *J. Opt. Soc. Am. B* **1993**, *10* (8), 1447−1456.

(22) Capretti, A.; Wang, Y.; Engheta, N.; Dal Negro, L. Comparative study of second-harmonic generation from epsilon-near-zero indium tin oxide and titanium nitride nanolayers excited in the near-infrared spectral range. *ACS Photonics* **2015**, *2* (11), 1584−1591.

(23) Cunha, R.; Cadore, A.; Ramos, S.; Watanabe, K.; Taniguchi, T.; Kim, S.; Solntsev, A. S.; Aharonovich, I.; Malard, L. M. Second harmonic generation in defective hexagonal boron nitride. *J. Phys.: Condens. Matter* **2020**, *32* (19), No. 19LT01.

(24) Yao, K.; Finney, N. R.; Zhang, J.; Moore, S. L.; Xian, L.; Tancogne-Dejean, N.; Liu, F.; Ardelean, J.; Xu, X.; Halbertal, D.; et al. Enhanced tunable second harmonic generation from twistable interfaces and vertical superlattices in boron nitride homostructures. *Sci. Adv.* **2021**, *7* (10), No. eabe8691.

(25) Li, Z.; Tudi, A.; Ren, P.; Yang, Y.; Iitaka, T.; Tohyama, T.; Yang, Z. H.; Pan, S. L.; Su, H. B. $NaPN_2$: Deep-ultraviolet nonlinear optical material with unprecedented strong second-harmonic generation coefficient. *Phys. Rev. Mater.* **2019**, *3*, No. 025201.

(26) Zhang, S.; Kang, L.; Lin, Z. Nonlinear optical ASnX (A = Na, H; X = N, P) nanosheets with divalent tin lone electron pair effect by first-principles design. *Nanoscale* **2020**, *12* (27), 14895−14902.

(27) Huang, J.; Shu, S.; Cai, G.-M. Screening nitrides with high debye temperatures as nonlinear optical materials. *J. Phys. Chem. C* **2022**, *126* (16), 7047−7053.

(28) Hellenbrandt, M. The inorganic crystal structure database (ICSD)—present and future. *Crystallogr. Rev.* **2004**, *10* (1), 17−22.
(29) Huang, J.; Xie, C.; Wei, L.; Bian, Q.; Yang, Z.; Pan, S. Predicting diamond-like nitrides as infrared nonlinear optical materials with high thermal conductivity. *Chem. Mater.* **2022**, *34* (22), 10059−10067.
(30) Chu, D.; Huang, Y.; Xie, C.; Tikhonov, E.; Kruglov, I.; Li, G.; Pan, S.; Yang, Z. Unbiased screening of novel infrared nonlinear optical materials with high thermal conductivity: long-neglected nitrides and popular chalcogenides. *Angew. Chem., Int. Ed.* **2023**, *62* (16), No. e202300581.
(31) Kloß, S. D.; Schnick, W. Nitridophosphates: a success story of nitride synthesis. *Angew. Chem., Int. Ed.* **2019**, *58* (24), 7933−7944.
(32) Landskron, K.; Schmid, S.; Schnick, W. Hochdruck-synthese, kristallstruktur und eigenschaften von $NaPN_2$. *Z. Anorg. Allg. Chem.* **2001**, *627* (11), 2469−2472.
(33) Pucher, F. J.; Hummel, F.; Schnick, W. $CuPN_2$: synthesis, crystal structure, and electronic properties. *Eur. J. Inorg. Chem.* **2015**, *2015* (11), 1886−1891.
(34) Eisenburger, L.; Weippert, V.; Paulmann, C.; Johrendt, D.; Oeckler, O.; Schnick, W. Discovery of two polymorphs of TiP_4N_8 synthesized from binary nitrides. *Angew. Chem., Int. Ed.* **2022**, *61* (19), No. e202202014.
(35) Pucher, F. J.; Marchuk, A.; Schmidt, P. J.; Wiechert, D.; Schnick, W. Luminescent nitridophosphates CaP_2N_4:Eu^{2+}, SrP_2N_4:Eu^{2+}, BaP_2N_4:Eu^{2+}, and $BaSr_2P_6N_{12}$:Eu^{2+}. *Chem. - Eur. J.* **2015**, *21* (17), 6443−6448.
(36) Jacobs, H.; Nymwegen, R. Darstellung und Kristallstruktur eines Kaliumnitridophosphats, K3P6N11. *Z. Anorg. Allg. Chem.* **1997**, *623* (1−6), 429−433.
(37) Ambach, S. J.; Pointner, M.; Falkai, S.; Paulmann, C.; Oeckler, O.; Schnick, W. Combining MN_6 octahedra and PN_5 trigonal bipyramids in the mica-like nitridophosphates MP_6N_{11}(M = Al, In). *Angew. Chem., Int. Ed.* **2023**, *62* (24), No. e202303580.
(38) Vogel, S.; Buda, A. T.; Schnick, W. United in nitride: the highly condensed boron phosphorus nitride BP_3N_6. *Angew. Chem., Int. Ed.* **2018**, *57* (40), 13202−13205.
(39) Pucher, F. J.; von Schirnding, C. F.; Hummel, F.; Celinski, V. R.; auf der Günne, J. S.; Gerke, B.; Pöttgen, R.; Schnick, W. $Sn_6P_{12}N_{24}$ − a sodalite-type nitridophosphate. *Eur. J. Inorg. Chem.* **2015**, *2015* (3), 382−388.
(40) de Boer, T.; Somers, C.; Boyko, T.; Ambach, S.; Eisenburger, L.; Schnick, W.; Moewes, A. The importance of lone pairs to structure and bonding of the novel germanium nitridophosphate GeP_2N_4. *J. Mater. Chem. A* **2023**, *11* (12), 6198−6204.
(41) Cheng, X.; Whangbo, M.-H.; Guo, G.-C.; Hong, M.; Deng, S. Large second harmonic generation of $LiCs_2PO_4$ caused by the metal-cation-centered groups. *Angew. Chem., Int. Ed.* **2018**, *57* (15), 3933−3937.
(42) Cheng, X.; Whangbo, M.-H.; Hong, M.; Deng, S. Dependence of the second-harmonic generation response on the cell volume to band-gap ratio. *Inorg. Chem.* **2019**, *58*, 9572−9575.
(43) Cheng, X.; Li, Z. H.; Wu, X.-T.; Hong, M.; Whangbo, M.-H.; Deng, S. Key factors controlling the large second harmonic generation in nonlinear optical materials. *ACS Appl. Mater. Interfaces* **2020**, *12* (8), 9434−9439.
(44) Batatia, I.; Kovacs, D. P.; Simm, G.; Ortner, C.; Csányi, G. In *MACE: Higher Order Equivariant Message Passing Neural Networks for Fast and Accurate Force Fields*, Advances in Neural Information Processing Systems; NeurIPS, 2022; pp 11423−11436.
(45) Deng, B.; Zhong, P.; Jun, K.; Riebesell, J.; Han, K.; Bartel, C. J.; Ceder, G. CHGNet as a pretrained universal neural network potential for charge-informed atomistic modelling. *Nat. Mach. Intell.* **2023**, *5* (9), 1031−1041.
(46) Stöwe, K.; Weber, M. Niobium, tantalum, and tungsten doped tin dioxides as potential support materials for fuel cell catalyst applications. *Z. Anorg. Allg. Chem.* **2020**, *646* (18), 1470−1480.
(47) Shannon, R. D. Revised effective ionic radii and systematic studies of interatomic distances in halides and chalcogenides. *Acta Crystallogr. A* **1976**, *32* (5), 751−767.
(48) Yao, W.-D.; Cheng, X.; Guo, S.-P.; Whangbo, M.-H.; Ding, B.; Deng, S. Phase competition and strong SHG responses of the $Li_2M^{II}M^{IV}Se_4$ family: atom response theory predictions versus experimental results. *Chem. Mater.* **2023**, *35* (3), 1159−1167.
(49) Jain, A.; Ong, S. P.; Hautier, G.; Chen, W.; Richards, W. D.; Dacek, S.; Cholia, S.; Gunter, D.; Skinner, D.; Ceder, G.; Persson, K. A. Commentary: the Materials Project: a materials genome approach to accelerating materials innovation. *APL Mater.* **2013**, *1* (1), No. 011002.
(50) Gonze, X.; Lee, C. Dynamical matrices, born effective charges, dielectric permittivity tensors, and interatomic force constants from density-functional perturbation theory. *Phys. Rev. B* **1997**, *55* (16), No. 10355.
(51) Veithen, M.; Gonze, X.; Ghosez, P. Nonlinear optical susceptibilities, raman efficiencies, and electro-optic tensors from first-principles density functional perturbation theory. *Phys. Rev. B* **2005**, *71*, No. 125107.
(52) Kurtz, S. K.; Perry, T. T. A powder technique for the evaluation of nonlinear optical materials. *J. Appl. Phys.* **1968**, *39* (8), 3798−3813.
(53) Cyvin, S. J.; Rauch, J. E.; Decius, J. C. Theory of hyper-raman effects (nonlinear inelastic light scattering): selection rules and depolarization ratios for the second-order polarizability. *J. Chem. Phys.* **1965**, *43* (11), 4083−4095.
(54) Dmitriev, V. G.; Gurzadyan, G. G.; Nikogosyan, D. N. *Handbook of Nonlinear Optical Crystals*; Springer, 1999.
(55) Tudi, A.; Han, S.; Yang, Z.; Pan, S. Potential optical functional crystals with large birefringence: Recent advances and future prospects. *Coord. Chem. Rev.* **2022**, *459*, No. 214380.
(56) Cheng, X.; Zhang, Y.; Liu, L.; Wang, X.; Whangbo, M. H.; Lin, J.; Deng, S. Structure and origin of the second-harmonic generation response of nonlinear optical material $Sr_2Be_2B_2O_7$. *J. Phys. Chem. Lett.* **2021**, *12*, 11399−11405.
(57) Perdew, J. P.; Burke, K.; Ernzerhof, M. Generalized gradient approximation made simple. *Phys. Rev. Lett.* **1996**, *77*, No. 3865.
(58) Kresse, G.; Hafner, J. *Ab initio* molecular dynamics for liquid metals. *Phys. Rev. B* **1993**, *47* (1), No. 558.
(59) Kresse, G.; Furthmüller, J. Efficiency of *ab-initio* total energy calculations for metals and semiconductors using a plane-wave basis set. *Comput. Mater. Sci.* **1996**, *6*, 15−50.
(60) Kresse, G.; Furthmüller, J. Efficient iterative schemes for *ab initio* total-energy calculations using a plane-wave basis set. *Phys. Rev. B* **1996**, *54* (16), No. 11169.
(61) Aversa, C.; Sipe, J. E. Nonlinear optical susceptibilities of semiconductors: results with a length-gauge analysis. *Phys. Rev. B* **1995**, *52* (20), No. 14636.
(62) Rashkeev, S. N.; Lambrecht, W. R. L. Second-harmonic generation of I-III-VI_2 chalcopyrite semiconductors: effects of chemical substitutions. *Phys. Rev. B* **2001**, *63* (16), No. 165212.
(63) Sharma, S.; Dewhurst, J. K.; Ambrosch-Draxl, C. Linear and second-order optical response of III-V monolayer superlattices. *Phys. Rev. B* **2003**, *67* (16), No. 165332.
(64) Sharma, S.; Ambrosch-Draxl, C. Second-harmonic optical response from first principles. *Phys. Scr.* **2004**, *T109*, 128−134.
(65) Krukau, A. V.; Vydrov, O. A.; Izmaylov, A. F.; Scuseria, G. E. Influence of the exchange screening parameter on the performance of screened hybrid functionals. *J. Chem. Phys.* **2006**, *125* (22), No. 224106.
(66) Togo, A.; Tanaka, I. First principles phonon calculations in materials science. *Scripta Mater.* **2015**, *108*, 1−5.
(67) Gonze, X.; Amadon, B.; Antonius, G.; Arnardi, F.; Baguet, L.; Beuken, J.-M.; Bieder, J.; Bottin, F.; Bouchet, J.; Bousquet, E.; et al. The Abinit project: Impact, environment and recent developments. *Comput. Phys. Commun.* **2020**, *248*, No. 107042.
(68) Romero, A. H.; Allan, D. C.; Amadon, B.; Antonius, G.; Applencourt, T.; Baguet, L.; Bieder, J.; Bottin, F.; Bouchet, J.; Bousquet, E.; et al. ABINIT: Overview and focus on selected capabilities. *J. Chem. Phys.* **2020**, *152* (12), No. 124102.

https://doi.org/10.1021/acs.chemmater.5c00109
Chem. Mater. 2025, 37, 3709−3719